Locomotion of Helical Bodies in Viscoelastic Fluids: Enhanced Swimming at Large Helical Amplitudes

Saverio E. Spagnolie*
Department of Mathematics, University of Wisconsin-Madison, 480 Lincoln Drive, Madison, Wisconsin 53706, USA

Bin Liu
School of Engineering, Brown University, 182 Hope Street, Providence, Rhode Island 02912, USA

Thomas R. Powers†
Department of Physics and School of Engineering, Brown University, 182 Hope Street, Providence, Rhode Island 02912, USA
(Received 20 February 2013; published 9 August 2013)

The motion of a rotating helical body in a viscoelastic fluid is considered. In the case of force-free swimming, the introduction of viscoelasticity can either enhance or retard the swimming speed and locomotive efficiency, depending on the body geometry, fluid properties, and the body rotation rate. Numerical solutions of the Oldroyd-B equations show how previous theoretical predictions break down with increasing helical radius or with decreasing filament thickness. Helices of large pitch angle show an increase in swimming speed to a local maximum at a Deborah number of order unity. The numerical results show how the small-amplitude theoretical calculations connect smoothly to the large-amplitude experimental measurements.

DOI: 10.1103/PhysRevLett.111.068101 PACS numbers: 47.63.−b, 87.17.Jj, 87.23.Kg

Much has been learned about the swimming of microorganisms in viscous environments over the last decade [1]. The peculiar behavior of complex fluids has also seen a recent burst of renewed interest, particularly as applied to biological systems. Progress in both fields has begun to blur together, since many organisms commonly swim in shear-thinning or viscoelastic fluids. Some of those fluids are complex specifically because of suspensions of microorganisms swimming and diffusing throughout [2–7]. Examples of microorganisms swimming in complex fluid environments include mammalian spermatozoa through cervical fluid [8], the Lyme disease spirochete *B. burgdorferi* through the extracellular matrix of our skin [9,10], and the nematode *C. elegans* in water-saturated soil [11]. Organisms such as *H. pylori* have even been found to reduce fluid elasticity in order to swim through mucus [12].

A puzzle has recently emerged in the study of swimming through complex fluids. Theory, experiment, and simulation have indicated the possibility of both enhancement and retardation of swimming speeds in viscoelastic fluids [see Figs. 1(a)–1(f)]. Helically shaped bacteria such as *Leptospira* [13] and *B. burgdorferi* swim faster in solutions with methylcellulose than in nonviscoelastic solutions of the same viscosity [9,14]. *C. elegans*, however, which propels itself by planar body undulations, swims slower in a viscoelastic fluid than in a viscous fluid [15]. Spermatozoan cells swim slower when the fluid has an elastic response, but along straighter paths due to resultant changes in the flagellar shape, with hyperactivated spermatozoan cells swimming faster than normal cells [16]. The consequences of fluid viscoelasticity on swimming is not, then, a question that can be answered broadly; effects appear to depend sensitively upon the geometry of the swimming stroke and the rheology of the complex fluid.

There have also been a number of recent analytical, numerical, and scale-model explorations. Analysis is commonly performed on the Oldroyd-B equations, which describe a viscoelastic flow with no shear thinning or thickening [17,18]. Using the Oldroyd-B model and others, Lauga showed that an infinite sheet passing small amplitude waves always swims slower with the introduction of viscoelasticity [19]. An identical factor of swimming speed reduction was recovered by Fu *et al*. for a nearly cylindrical body of small pitch angle when passing helical waves [20], and similarly for the passage of planar waves [21]. Teran *et al*. showed that finite undulatory bodies of large wave amplitude can swim faster in a viscoelastic fluid [22], while Curtis and Gaffney showed the same for a three-sphere swimmer [23], as did Espinosa-Garcia *et al*. for flexible swimmers [24]. Finally, Liu *et al*. studied experimentally the motion of a rotating, force-free helical filament in a (viscoelastic) Boger fluid, finding that the swimming speed increased or decreased with viscoelasticity depending on the body geometry and rotation rate [see Fig. 1(f)] [25]. Other investigations have shown increases or decreases in speed depending on fluid properties [26].

In this Letter we bridge the gap between the analytical predictions and the experimental and numerical observations just described. By studying numerically the swimming of a helical body in an Oldroyd-B model fluid, we show that the theoretical efforts do indeed capture the effects of viscoelasticity when the helical pitch angle is

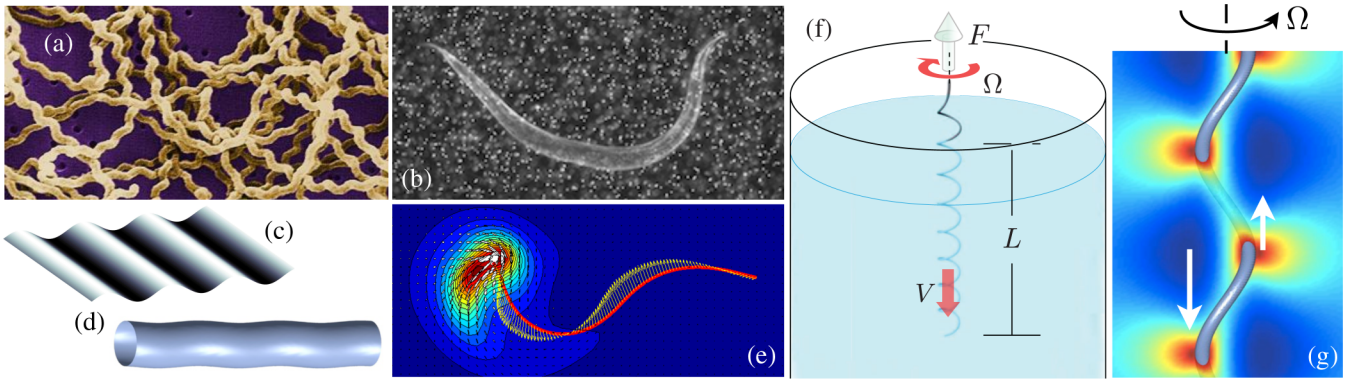

FIG. 1 (color online). Experiments, theories, and simulations of swimming in viscoelastic fluids. With increasing fluid elasticity, (a) the helical bacterium *Leptospira* swims faster (see also Fig. 7 of Ref. [13], courtesy of J. H. Carr, CDC, 2103) [9,14]; (b) the nematode *C. elegans* swims slower [15] (courtesy of X. N. Shen and P. E. Arratia, 2013); (c) a two-dimensional swimming sheet of small wave amplitude swims slower [19]; (d) a nearly cylindrical swimmer passing helical waves of small pitch angle swims slower with the same factor of reduction as for the two-dimensional sheet [20]; (e) a finite undulatory swimmer swims faster for a range of beating frequencies (instantaneous body velocity and mean-squared polymer distention field are shown [22], courtesy of J. Teran, L. Fauci, and M. Shelley, 2013); (f) and a thin helical body of arbitrary length can swim faster or slower, depending on the geometry and rotation rate [25]. (g) The axial component of fluid velocity generated by a rotating, force-free helical filament is shown; a helical fluid volume external to the coil is carried upward with the translating body, while a helical fluid volume internal to the coil is shuttled downward.

small and the filament radius is large: namely, that the swimming speed of a rotating helical body in this regime is always smaller than the same in a Newtonian fluid. We will then show how these theories break down for helices of large pitch angle and that the swimming speed can increase with the introduction of viscoelasticity. The results may improve our understanding of mammalian fertility and the spread of bacterial infections and diseases [10].

The Letter is organized as follows. We begin by presenting the mathematical model of a rotating, force-free helical body in an Oldroyd-B fluid, followed by a dimensional analysis and a description of the numerical method. Helices of small pitch angle are explored, for which we show a continuous departure of the small amplitude analytical theories from the results of the full model. We then turn to helices of large pitch angle where fluid elasticity is shown to increase the swimming speed to a local maximum at a Deborah number of order unity. Both helical waves and rigid body rotations are considered, and the locomotive efficiency is addressed. We conclude with a summary and a discussion of future directions.

The experiments of Liu *et al*. suggest that the force-free swimming speed of a helical filament is broadly independent of its length [25]. We therefore consider a right-handed helical body of infinite length with centerline $\boldsymbol{x}(s,t) = b[\cos(ks + \Omega t)\hat{\boldsymbol{x}} + \sin(ks + \Omega t)\hat{\boldsymbol{y}}] + ([1 - (bk)^2]^{1/2}s + U^*t)\hat{\boldsymbol{z}}$. Here, b is the helical radius, k is the wave number, s is the arc length, Ω is a fixed rotation rate, and U^* is the swimming speed. The body is shaped such that the boundary in a cross-sectional plane perpendicular to the $\hat{\boldsymbol{z}}$ axis is circular with radius A/k. The distinction between helical waves and rigid body rotation is a rotation of this circle about the centerline in the latter.

At the length and velocity scales relevant for microorganisms, viscous effects dominate inertial effects [1] and the momentum and mass conservation equations are $\nabla p = \nabla \cdot \boldsymbol{\tau}$ and $\nabla \cdot \boldsymbol{u} = 0$, where p is the pressure and $\boldsymbol{\tau}$ is the total deviatoric stress tensor. In the Oldroyd-B model, $\boldsymbol{\tau}$ is the sum of a Newtonian solvent contribution, $\boldsymbol{\tau}_s = \eta_s\dot{\boldsymbol{\gamma}}$, and an extra polymeric contribution, $\boldsymbol{\tau}_p$, where η_s is the solvent viscosity, $\dot{\boldsymbol{\gamma}} = \nabla\boldsymbol{u} + \nabla\boldsymbol{u}^T$ is the rate-of-strain tensor, and $\boldsymbol{u}$ is the fluid velocity. Meanwhile, $\boldsymbol{\tau}_p$ is described by an upper-convected Maxwell model in which a single elastic relaxation time scale, λ_1, and a viscous retardation time scale, λ_2, are introduced (with $\lambda_2 = \lambda_1\eta_s/\eta < \lambda_1$ and η the total zero shear rate viscosity) [17,18]. Scaling lengths on $1/k$, time on $1/\Omega$, velocities on Ω/k, and stresses on $\eta\Omega$, the total deviatoric stress is found to satisfy the dimensionless constitutive relation,

$$\boldsymbol{\tau} + \mathrm{De}\,\overset{\triangledown}{\boldsymbol{\tau}} = \dot{\boldsymbol{\gamma}} + (\eta_s/\eta)\mathrm{De}\,\overset{\triangledown}{\dot{\boldsymbol{\gamma}}}. \tag{1}$$

Here we have defined the dimensionless Deborah number, $\mathrm{De} = \lambda_1\Omega$, which compares the body rotation rate to the rate of elastic relaxation. The upper convective time derivative in Eq. (1) is defined as $\overset{\triangledown}{\boldsymbol{\tau}} = \boldsymbol{\tau}_t + \boldsymbol{u}\cdot\nabla\boldsymbol{\tau} - \nabla\boldsymbol{u}^T\cdot\boldsymbol{\tau} - \boldsymbol{\tau}\cdot\nabla\boldsymbol{u}$. More complex models include features such as multiple relaxation time scales and finite polymer extensibility [17].

The Deborah numbers relevant to microorganism motility are likely to span a very wide range. Relaxation times of cervical mucus have been measured from $\lambda_1 = 0.03$ s to $\lambda_1 = 100$ s; spermatozoa in this environment undulate with frequencies between 20 and 50 Hz, corresponding to Deborah numbers that are $O(1)$ or much larger (see Refs. [19,27]). An intriguing example of Deborah number

variation is exhibited in the swimming of *H. pylori*, which rotates a helical flagellum at up to 5 Hz in viscoelastic mucus with a relaxation time of approximately 100 s, but releases *p*H-increasing urease enzymes that decrease the local relaxation time to nearly 0.05 s, thereby decreasing the Deborah number from $O(1000)$ to $O(1)$ [12].

Due to the interaction with the fluid, the helical filament translates along the axial direction with dimensionless speed U, as illustrated in Fig. 2(a). A no-slip condition is assumed on the body surface, and for computational purposes we place the filament inside a very large container where we set $\boldsymbol{u} = 0$. The container is made sufficiently large so that further increases in its size have a negligible effect on the reported results. The problem is closed by requiring that the axial component of force on the body is zero. The constant swimming speed U is determined by assuming that a locomotive steady state has been achieved and by exploiting helical symmetry: the flow and stress fields everywhere are given by translation and rotation of the flow field through the $z = 0$ plane. Conversion to a helical coordinate system allows for z derivatives to be written as planar derivatives on $z = 0$. In a periodic steady state, time derivatives may be written as z derivatives, and hence by planar derivatives as well. The Oldroyd-B equations are solved numerically using a mixed pseudo-spectral and finite differences approach. The mathematical model and numerical method are described in greater detail in the Supplemental Material [28].

We first compare the numerical results to the analytical work of Fu *et al.* [20] in the case of a helical wave with a small pitch angle. For $\psi = \pi/40$, the normalized swimming speed is shown in Fig. 2(b) for a range of Deborah numbers and filament sizes. Here as in the remainder of the Letter we fix the viscosity ratio to $\eta_s/\eta = 0.5$. Each solid line corresponds to a different filament radius, $A = 2^{n-2}$, for $n = 0, 1, \ldots, 6$. By increasing the filament thickness the swimming speed converges monotonically to the analytical result, shown as a dashed line. Viscoelasticity in this case decreases the swimming speed of helices with small pitch angles, even for slender bodies, contrasting with the enhanced speeds predicted in a viscous fluid in the presence of stationary obstacles [29]. The departure of the results from the analytical theory are logarithmic in A, consistent with the analytical development [20].

The analytical results for small pitch angles have been recovered, but can the increased swimming speeds seen in experiments be found? Figure 2(c) shows the normalized swimming speed as a function of the Deborah number for

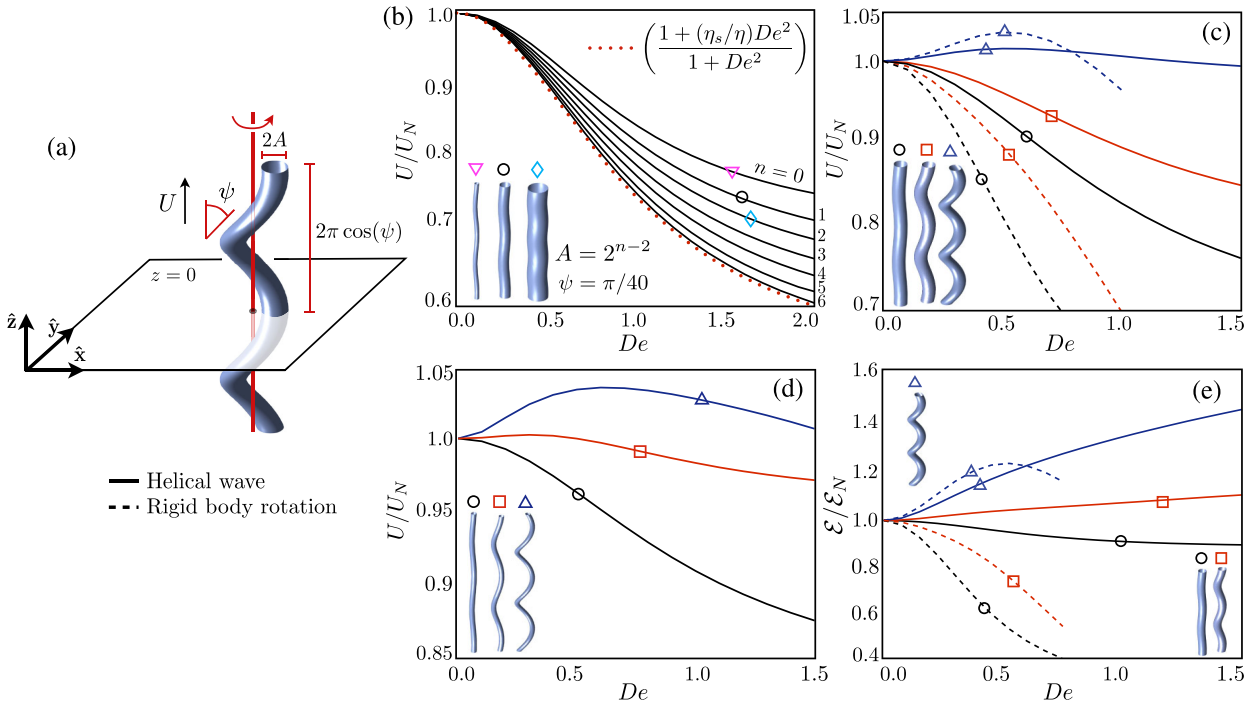

FIG. 2 (color online). (a) Schematic of the dimensionless setup. The body rotates counterclockwise with unit angular speed when seen from above and swims in the axial direction with dimensionless speed U. (b) Helical-wave swimming speed (normalized by the Newtonian swimming speed) of filaments of varying thickness, $A = 2^{n-2}$. Here $\psi = \pi/40$ and $\eta_s/\eta = 0.5$. Deviations from the theoretical result of Fu *et al.* [20] (dotted line) are logarithmic in A. (c) Viscoelasticity leads to faster swimming for helices of a sufficiently large pitch angle. The filament thickness is fixed, $A = 0.5$. Solid lines denote helical waves, dashed lines denote rigid body rotation, and symbols denote pitch angle, $\psi = \pi/40$, $\pi/10$, and $\pi/5$. (d) Larger swimming speeds are achieved by thinner filaments of the same pitch angles as in (c); here $A = 0.2$. (e) The normalized swimming efficiency for helical waves and rigid body rotations. Symbols denote the same helices as in (c).

three different pitch angles, $\psi = \pi/40$, $\pi/10$, and $\pi/5$, with $A = 0.5$. Helical wave and rigid body rotation results are shown as solid and dashed lines, respectively. For small Deborah numbers we observe $U/U_N = 1 + O(\mathrm{De}^2)$, as required by symmetry. In both cases, for a given Deborah number in the regime considered, the swimming speed increases as the pitch angle is increased to $\psi = \pi/5$. Moreover, beyond a critical pitch angle we find a range of Deborah numbers for which the swimming speed is larger in a viscoelastic fluid than in a Newtonian fluid, just as observed in experiments [25].

Rigid body motion, which generates an extra rotational flow around the helical filament as compared to helical waves, amplifies the effects of viscoelasticity, particularly for small pitch angles where rotational flow is dominant. Viscoelastic effects are amplified with decreasing η_s/η as well (not shown). Filament thickness is also important; Fig. 2(d) shows the helical-wave swimming speeds of slender filaments ($A = 0.2$), which are greater than those shown in Fig. 2(c). In particular, for the intermediate pitch angle $\psi = \pi/10$, reducing the filament thickness introduces a regime in a small Deborah number for which the relative swimming speed is greater than unity.

A microorganism may benefit by swimming with greater efficiency rather than greater speed. We evaluate a common measure of swimming efficiency, $\mathcal{E} = U^2/P$, where $P = (1/2)\int_{z=0} \dot{\boldsymbol{\gamma}}:\boldsymbol{\tau} dS$ is the rate of energy dissipation in the fluid per unit length [19,20,22]. The results are shown in Fig. 2(e) for the same helical shapes considered in Fig. 2(c). An important distinction between the passage of helical waves and rigid body rotation is observed. For rigid body rotation, the work done on the fluid does not vary dramatically with the Deborah number; just as was found for planar undulations, the swimming speed is a proxy for swimming efficiency in the case of rigid body rotation [22]. The rotation of helices of large pitch angle therefore presents a means of swimming that is both faster and more efficient in a viscoelastic fluid when the rotation rate is properly tuned to the fluid environment. For helical waves, however, the swimming speed is not so clearly linked to the efficiency; for $\psi = \pi/10$ the relative swimming speed decreases with De while the relative efficiency increases. By inspection of the no-slip boundary condition, the differences between rigid body rotation and helical waves are expected to diminish rapidly with both decreasing filament size and increasing pitch angle.

The effects of viscoelasticity on the swimming of helices are not easily predicted by thought experiments. The flow field created by a rotating helix in a Newtonian fluid is intricate; the extra polymeric stresses that develop due to this flow field, the response of the flow field to the polymeric stresses, and the interaction of solvent and polymeric forces with the helix all provide for a complex and highly nonlinear system.

We do, however, observe a distinction in the polymeric stresses between cases where viscoelasticity either reduces or increases the swimming speed. Consider the spatial distribution of $\mathrm{tr}(\boldsymbol{\tau}_p)$ for the passage of helical waves along two different helical geometries. This quantity measures the mean-squared distention of the elastic polymers, and is shown for helices of small and large pitch angle in Fig. 3. For small Deborah numbers, the polymers are stretched most in regions of large fluid shear, which are at the leftmost and rightmost points of the circular boundaries in Fig. 3 (the inner and outer edges of the filament, respectively). Fluid shear is largest in these regions due not only to the motion of the filament through the $z = 0$ plane, but also to the arrangement of the axial fluid velocity, as shown for $\mathrm{De} = 0$ in Fig. 1(g).

Increasing the Deborah number, however, shows a distinct difference in the organization of polymeric stress in these two cases. For the helix of smaller pitch angle the primary regions of extra stress rotate clockwise. As these regions are displaced, they affect the underlying flow field, and both conspire to reduce the filament swimming speed. For the helix of larger pitch angle, however, we observe the opposite shift: extra polymeric stresses have shifted counterclockwise. Much as in the case of flow past a cylinder, the reorganization of elastic fluid stress acts to shift the distribution of pressure, which further contributes to adjustments in both vertical and horizontal fluid forces on the body [30].

Recall that a Deborah number of order unity indicates a helical rotation rate comparable to the rate of elastic relaxation. When $\mathrm{De} \approx 1$, polymers distended by the motion of the body release stored elastic energy on a special time

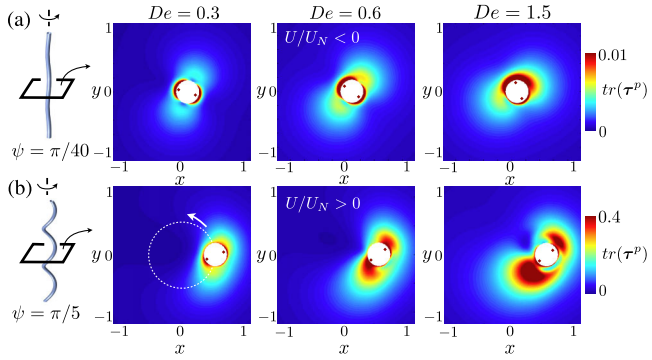

FIG. 3 (color online). The mean-squared polymer distention fields, $\mathrm{tr}(\boldsymbol{\tau}_p)$, from the passage of helical waves are shown for three Deborah numbers, for filament thickness $A = 0.2$ and pitch angles (a) $\psi = \pi/40$ and (b) $\psi = \pi/5$. The swimming speed decreases with the Deborah number in (a) and increases in (b). The path of the body during rotation is indicated by a white dashed line in the bottom left panel. The largest polymer distention appears along the second and fourth quadrants in case (a), and along the first and third quadrants in case (b), with the regions of maximal distention indicated by symbols.

scale. Namely, a time scale such that the body can revisit the viscoelastic wake created on each pass through the same location. For helices of small pitch angle, the motion of the body in the $z = 0$ plane is muted, and fluid parcels do not make large excursions in the plane. With a larger pitch angle, the filament travels on a much wider circuit relative to its thickness, the body can interact with its own viscoelastic wake, and elastic stresses can be transmitted from the wake back onto the body upon its return. This heuristic also suggests that a smaller filament thickness (with pitch angle fixed) may lead to increased swimming speeds, as we have already observed in Fig. 2(d).

We have shown that the introduction of viscoelasticity can either decrease or increase the force-free swimming speed and swimming efficiency of a rotating helical filament, depending on the helical geometry, the material properties of the fluid, and the body rotation rate. The results of our investigation connect the small amplitude theories, experimental observations, and numerical investigations of the biological and mechanical experiments shown in Fig. 1. Our findings may add context to the recent discovery that *H. pylori* reduces mucus elasticity to a range more suitable for effective locomotion [12]. Future work will explore the effects of viscoelasticity on the propulsion of elastic helical filaments, on flagellar bundling, and on more intricate biological structures such as those relevant to bacterial polymorphism [31–33]. Similar behaviors are expected in a nearby fluid pumping problem, where fluid is transported downward either faster or slower than the same in a Newtonian setting.

We acknowledge helpful discussions with M. D. Graham, M. J. Shelley, R. H. Ewoldt, and M. G. Forest, and we are especially grateful to K. S. Breuer for ongoing collaboration. This work was supported by the NSF Grant No. CBET-0854108.

*spagnolie@math.wisc.edu
†thomas_powers@brown.edu

[1] E. Lauga and T. R. Powers, Rep. Prog. Phys. **72**, 096601 (2009).
[2] T. J. Pedley and J. O. Kessler, Annu. Rev. Fluid Mech. **24**, 313 (1992).
[3] Y. Hatwalne, S. Ramaswamy, M. Rao, and R. A. Simha, Phys. Rev. Lett. **92**, 118101 (2004).
[4] T. Ishikawa and T. J. Pedley, J. Fluid Mech. **588**, 399 (2007).
[5] A. Sokolov and I. S. Aranson, Phys. Rev. Lett. **103**, 148101 (2009).
[6] S. Rafaï, L. Jibuti, and P. Peyla, Phys. Rev. Lett. **104**, 098102 (2010).
[7] G. Foffano, J. S. Lintuvuori, A. N. Morozov, K. Stratford, M. E. Cates, and D. Marenduzzo, Eur. Phys. J. E **35**, 1 (2012).
[8] S. S. Suarez and A. A. Pacey, Human Reprod. Update **12**, 23 (2006).
[9] R. B. Kimsey and A. Spielman, J. Infect. Dis. **162**, 1205 (1990).
[10] M. W. Harman, S. M. Dunham-Ems, M. J. Caimano, A. A. Belperron, L. K. Bockenstedt, H. C. Fu, J. D. Radolf, and C. W. Wolgemuth, Proc. Natl. Acad. Sci. U.S.A. **109**, 3059 (2012).
[11] S. Jung, Phys. Fluids **22**, 031903 (2010).
[12] J. P. Celli *et al.*, Proc. Natl. Acad. Sci. U.S.A. **106**, 14 321 (2009).
[13] A. R. Bharti *et al.*, Lancet Infect. Dis. **3**, 757 (2003).
[14] H. C. Berg and L. Turner. Nature (London) **278**, 349 (1979).
[15] X. N. Shen and P. E. Arratia, Phys. Rev. Lett. **106**, 208101 (2011).
[16] S. S. Suarez and X. Dai, Biol. Reprod. **46**, 686 (1992).
[17] R. B. Bird, R. C. Armstrong, and O. Hassager, *Dynamics of Polymeric Liquids*, Fluid Mechanics Vol. 1 (John Wiley and Sons, New York, NY, 1987).
[18] R. G. Larson, *The Structure and Rheology of Complex Fluids* (Oxford University Press, New York, 1999), Vol. 1.
[19] E. Lauga, Phys. Fluids **19**, 083104 (2007).
[20] H. C. Fu, C. W. Wolgemuth, and T. R. Powers, Phys. Fluids **21**, 033102 (2009).
[21] H. C. Fu, T. R. Powers, and H. C. Wolgemuth, Phys. Rev. Lett. **99**, 258101 (2007).
[22] J. Teran, L. Fauci, and M. Shelley, Phys. Rev. Lett. **104**, 038101 (2010).
[23] M. P. Curtis and E. A. Gaffney, Phys. Rev. E **87**, 043006 (2013).
[24] J. Espinosa-Garcia, E. Lauga, and R. Zenit, Phys. Fluids **25**, 031701 (2013).
[25] B. Liu, T. R. Powers, and K. S. Breuer, Proc. Natl. Acad. Sci. U.S.A. **108**, 19 516 (2011).
[26] M. Dasgupta, B. Liu, H. C. Fu, M. Berhanu, K. S. Breuer, T. R. Powers, and A. Kudrolli, Phys. Rev. E **87**, 013015 (2013).
[27] D. J. Smith, E. A. Gaffney, H. Gadêlha, N. Kapur, and J. C. Kirkman-Brown, Cell Motil. Cytoskeleton **66**, 220 (2009).
[28] See Supplemental Material at http://link.aps.org/supplemental/10.1103/PhysRevLett.111.068101 for details on the mathematical formulation, numerical method, and experimental data.
[29] A. M. Leshansky, Phys. Rev. E **80**, 051911 (2009).
[30] N. Phan-Thien and H. S. Dou, Comput. Methods Appl. Mech. Eng. **180**, 243 (1999).
[31] C. R. Calladine, Nature (London) **255**, 121 (1975).
[32] S. V. Srigiriraju and T. R. Powers, Phys. Rev. Lett. **94**, 248101 (2005).
[33] S. E. Spagnolie and E. Lauga, Phys. Rev. Lett. **106**, 058103 (2011).

Locomotion of Helical Bodies in Viscoelastic Fluids: Enhanced Swimming at Large Helical Amplitudes
Supplementary material

Saverio E. Spagnolie*
Department of Mathematics, University of Wisconsin-Madison, 480 Lincoln Drive, Madison, WI 53706, USA

Bin Liu
School of Engineering, Brown University, 182 Hope Street, Providence, RI 02912, USA

Thomas R. Powers
Department of Physics and School of Engineering, Brown University, 182 Hope Street, Providence, RI 02912, USA

(Dated: August 9, 2013)

In this document we describe in greater detail the numerical method used for the study described in the primary text, and tabulate a selection of rheological measurements and microorganism geometries relevant to our investigation. In §I the filament geometry and the Oldroyd-B equations are written in a helical coordinate system. The numerical discretization and method of solution are then described; numerous differential operations in the helical coordinate system are included in an accompanying appendix. In §II we provide the measured fluid rheologies and biological data from recent experiments.

I. NUMERICAL METHOD

Filament geometry and nondimensionalization

In our investigation the Stokes/Oldroyd-B equations are solved numerically in a cross-sectional plane of an infinitely long, rotating helical filament. A material point on the filament centerline is described in the fixed lab frame by

$$\boldsymbol{x}_0(s,t) = b[\cos(ks+\Omega t)\hat{\boldsymbol{x}} + \sin(ks+\Omega t)\hat{\boldsymbol{y}}] + (\alpha s + U^* t)\,\hat{\boldsymbol{z}}, \tag{1}$$

where b is the helical radius, k is the wavenumber, Ω is a fixed rotation rate, and U^* is the swimming speed. The parameter s is made the arc-length by setting $\alpha = \sqrt{1-(bk)^2}$. The body is shaped such that the boundary in a cross-sectional plane perpendicular to the $\hat{\boldsymbol{z}}$ axis is circular with radius A/k. Scaling velocities on Ω/k, lengths on $1/k$, and time upon $1/\Omega$, the dimensionless filament centerline is given by

$$\boldsymbol{x_0}(s,t) = \beta\,[\cos(s+t)\hat{\boldsymbol{x}} + \sin(s+t)\hat{\boldsymbol{y}}] + (\alpha s + Ut)\,\hat{\boldsymbol{z}}, \tag{2}$$

with $\beta = bk$ (hence $\alpha^2+\beta^2 = 1$) and $U = U^*k/\Omega$, where all variables are understood to be dimensionless. In the main text we described the geometry in terms of the pitch angle, ψ, with $(\alpha,\beta) = (\cos(\psi),\sin(\psi))$.

We now describe a time-dependent, helical coordinate system (r,θ,ζ) that conforms to the helical body as it translates with constant dimensionless speed U and rotates with unit angular velocity through the fluid. Defining the unit vectors $(\hat{\mathbf{x}}(\zeta,t),\hat{\mathbf{y}}(\zeta,t))$, which rotate and translate along with the body, a point in space is

written as

$$\boldsymbol{x} = (\beta + r\cos(\theta))\,\hat{\mathbf{x}}(\zeta, t) + r\sin(\theta)\,\hat{\mathbf{y}}(\zeta, t) + (\zeta + Ut)\,\hat{\boldsymbol{z}}, \tag{3}$$

$$\hat{\mathbf{x}}(\zeta, t) = \cos(\zeta/\alpha + t)\hat{\boldsymbol{x}} + \sin(\zeta/\alpha + t)\hat{\boldsymbol{y}}, \tag{4}$$

$$\hat{\mathbf{y}}(\zeta, t) = -\sin(\zeta/\alpha + t)\hat{\boldsymbol{x}} + \cos(\zeta/\alpha + t)\hat{\boldsymbol{y}}, \tag{5}$$

where r is the (dimensionless) distance from the filament centerline in the plane perpendicular to $\hat{\boldsymbol{z}}$ (a plane of constant ζ). Holding (r, θ) fixed, the line parameterized by ζ is helical and periodic on $\zeta \in [0, 2\pi\alpha]$; holding $r = A$ fixed, the material filament surface is parameterized by (ζ, θ). A polar coordinate system (r, θ) is used to parameterized space in a cross-sectional plane of the helical body, where

$$\hat{\boldsymbol{r}} = \cos(\theta)\hat{\mathbf{x}} + \sin(\theta)\hat{\mathbf{y}}, \quad \hat{\boldsymbol{\theta}} = -\sin(\theta)\hat{\mathbf{x}} + \cos(\theta)\hat{\mathbf{y}}. \tag{6}$$

The velocity boundary conditions for rigid body motion (applying the no-slip condition) are then written as

$$\boldsymbol{u}(r = A, \theta, \zeta) = -A\sin(\theta)\,\hat{\mathbf{x}} + (\beta + A\cos(\theta))\,\hat{\mathbf{y}} + U\hat{\boldsymbol{z}} = \beta\sin(\theta)\hat{\boldsymbol{r}} + (A + \beta\cos(\theta))\hat{\boldsymbol{\theta}} + U\hat{\boldsymbol{z}}, \tag{7}$$

with the ζ dependence implicit in the definitions of $\hat{\boldsymbol{r}}$ and $\hat{\boldsymbol{\theta}}$, while the passage of a helical wave requires instead that

$$\boldsymbol{u}(r = A, \theta, \zeta) = \beta\,\hat{\mathbf{y}} + U\hat{\boldsymbol{z}} = \beta\sin(\theta)\hat{\boldsymbol{r}} + \beta\cos(\theta)\hat{\boldsymbol{\theta}} + U\hat{\boldsymbol{z}}. \tag{8}$$

The boundary conditions differ by an extra rotation about the filament centerline in the former, with diminishing consequences for decreasing A/β.

Oldroyd-B equations in the helical coordinate system

Given that the helical filament is of infinite length, the steady-state (with respect to the body frame) is instantaneously described by the velocity and stress fields in any cross-sectional plane perpendicular to $\hat{\boldsymbol{z}}$. As described in the main text, in the fluid domain we solve the Oldroyd-B equations in the Stokes limit,

$$\nabla p = \nabla \cdot \boldsymbol{\tau}, \tag{9}$$

$$\nabla \cdot \boldsymbol{u} = 0, \tag{10}$$

where $\boldsymbol{u}$ is the fluid velocity, p is the pressure, and $\boldsymbol{\tau}$ is the total (deviatoric) viscoelastic stress tensor, $\boldsymbol{\tau} = \eta_s\dot{\boldsymbol{\gamma}} + \boldsymbol{\tau}_p$. Here η_s is the solvent viscosity, $\dot{\boldsymbol{\gamma}} = \nabla\boldsymbol{u} + \nabla\boldsymbol{u}^T$ is the rate-of-strain tensor, and $\boldsymbol{\tau}_p$ is the extra stress contributed by the polymer suspension. In the Newtonian case, where $\boldsymbol{\tau}_p = 0$, the divergence of the stress reduces to $\nabla \cdot \boldsymbol{\tau} = \eta_s\Delta\boldsymbol{u}$. In the Oldroyd-B model, the polymer stress is given by

$$\boldsymbol{\tau}_p + \lambda_1\overset{\triangledown}{\boldsymbol{\tau}}_p = \eta_p\dot{\boldsymbol{\gamma}}, \tag{11}$$

where η_p is the polymer suspension viscosity, $\eta = \eta_s + \eta_p$ is the total viscosity, and λ_1 is the polymer relaxation time-scale [1, 2]. The upper convective time derivative is defined by

$$\overset{\triangledown}{\boldsymbol{\tau}} = \boldsymbol{\tau}_t + \boldsymbol{u} \cdot \nabla\boldsymbol{\tau} - \nabla\boldsymbol{u}^T \cdot \boldsymbol{\tau} - \boldsymbol{\tau} \cdot \nabla\boldsymbol{u}. \tag{12}$$

Manipulation of Eqn. (11) leads to an equation for the total stress, $\boldsymbol{\tau}$,

$$\boldsymbol{\tau} + \lambda_1\overset{\triangledown}{\boldsymbol{\tau}} = \eta\left(\dot{\boldsymbol{\gamma}} + \lambda_2\overset{\triangledown}{\dot{\boldsymbol{\gamma}}}\right), \tag{13}$$

with $\lambda_2 = (\eta_s/\eta)\lambda_1$. Scaling time on $1/\Omega$, velocities on Ω/k and stresses on $\eta\,\Omega$, we find the dimensionless constitutive relation as stated in the main text,

$$\boldsymbol{\tau} + \mathrm{De}\,\overset{\triangledown}{\boldsymbol{\tau}} = \dot{\boldsymbol{\gamma}} + (\eta_s/\eta)\mathrm{De}\,\overset{\triangledown}{\dot{\boldsymbol{\gamma}}}, \tag{14}$$

and $\boldsymbol{\tau} = (\eta_s/\eta)\dot{\boldsymbol{\gamma}} + \boldsymbol{\tau}_p$. The Deborah number compares the rate of rotation to the rate of elastic relaxation in the fluid, $\mathrm{De} = \lambda_1\Omega$. Once again, all variables are understood to be dimensionless in the above. The dimensionless momentum balance equation (9) is then given by

$$\nabla p = (\eta_s/\eta)\boldsymbol{\Delta u} + \nabla\cdot\boldsymbol{\tau}_p, \tag{15}$$

Note that in the limit of $\mathrm{De}\to 0$, we have $\boldsymbol{\tau}_p = (1-(\eta_s/\eta))\dot{\boldsymbol{\gamma}}$, $\boldsymbol{\tau} = \dot{\boldsymbol{\gamma}}$, and $\nabla p = \nabla\cdot\boldsymbol{\tau} = \boldsymbol{\Delta u}$ as expected. Finally, the dimensionless fluid force per wavelength acting axially (in the $\hat{\boldsymbol{z}}$ direction) at any time or station in z is given by

$$F_z = 2\pi\alpha A\int_0^{2\pi}\left[(\beta/\alpha)\sin(\theta)(p-\tau_{zz})+\tau_{rz}\right]_{r=A}d\theta. \tag{16}$$

Exploiting helical symmetry

Under the transformation to helical coordinate system shown in (3), we have

$$\frac{\partial}{\partial \mathsf{x}} = \cos(\theta)\frac{\partial}{\partial r} - \frac{1}{r}\sin(\theta)\frac{\partial}{\partial\theta}, \tag{17}$$

$$\frac{\partial}{\partial \mathsf{y}} = \sin(\theta)\frac{\partial}{\partial r} + \frac{1}{r}\cos(\theta)\frac{\partial}{\partial\theta}, \tag{18}$$

$$\frac{\partial}{\partial z} = \frac{\partial}{\partial\zeta} - \frac{1}{\alpha}\left(\left[1+\frac{\beta\cos(\theta)}{r}\right]\frac{\partial}{\partial\theta} + \beta\sin(\theta)\frac{\partial}{\partial r}\right). \tag{19}$$

Consider a steady-state with respect to the body frame. Invoking helical symmetry, for any scalar quantity Φ we have that $\partial\Phi/\partial\zeta = 0$. Equation (19) then shows how an axial (z) derivative may be written solely in terms of r and θ derivatives. Hence, it is straightforward to show that the del operator may be written as

$$\nabla = \hat{\mathbf{x}}\partial_{\mathsf{x}} + \hat{\mathbf{y}}\partial_{\mathsf{y}} + \hat{\boldsymbol{z}}\partial_z = \hat{\boldsymbol{r}}\partial_r + \hat{\boldsymbol{\theta}}\frac{1}{r}\partial_\theta + \hat{\boldsymbol{z}}\left[-\frac{1}{\alpha}\left(\left[1+\frac{\beta\cos(\theta)}{r}\right]\partial_\theta + \beta\sin(\theta)\partial_r\right)\right], \tag{20}$$

(see Appendix A). The gradient of any scalar variable such as the pressure is then given simply by

$$\nabla p = \hat{\boldsymbol{r}}\frac{\partial p}{\partial r} + \hat{\boldsymbol{\theta}}\frac{1}{r}\frac{\partial p}{\partial\theta} + \hat{\boldsymbol{z}}\frac{\partial p}{\partial z}, \tag{21}$$

where

$$\frac{\partial p}{\partial z} = -\frac{1}{\alpha}\left(\left[1+\frac{\beta\cos(\theta)}{r}\right]\frac{\partial p}{\partial\theta} + \beta\sin(\theta)\frac{\partial p}{\partial r}\right). \tag{22}$$

Similarly, the divergence of a vector field $\boldsymbol{u} = u\hat{\boldsymbol{r}} + v\hat{\boldsymbol{\theta}} + w\hat{\boldsymbol{z}}$ is given by

$$\nabla\cdot\boldsymbol{u} = \frac{\partial u}{\partial r} + \frac{1}{r}\left(\frac{\partial v}{\partial r} + u\right) + \frac{\partial w}{\partial z}, \tag{23}$$

where again $\partial w/\partial z$ is written in terms of only r and θ derivatives. Numerous differential operations in the helical coordinate system are included in Appendix A.

A final simplification comes with the consideration of time-derivatives. For this simplification, we choose to solve the equations of motion in a translating plane of constant $z' = z + (\alpha - U)t$, or equivalently for constant $\zeta' = \zeta + \alpha t$, in which the filament geometry (though not material) appears to be fixed in space. The equations of motion go unchanged in the translating frame as a consequence of Galilean invariance. Assuming a steady state of flow and stress relative to the body geometry we have for any scalar function $\Phi(\boldsymbol{x}, t)$ that

$$0 = \frac{d}{dt}\Phi(\boldsymbol{x}, t)\Big|_{r,\theta,\zeta'} = \Phi_t + \boldsymbol{x}_t \cdot \nabla\Phi\Big|_{r,\theta,\zeta'}, \tag{24}$$

with subscripts denoting partial derivatives. A partial time derivative may therefore be written in terms of spatial derivatives confined to a plane of constant ζ',

$$\Phi_t\Big|_{r,\theta,\zeta'} = (\alpha - U)\Phi_z\Big|_{r,\theta,\zeta'} = \left(\frac{U}{\alpha} - 1\right)\left(\left[1 + \frac{\beta\cos(\theta)}{r}\right]\Phi_\theta + \beta\sin(\theta)\Phi_r\right)\Big|_{r,\theta,\zeta'}. \tag{25}$$

Discretization and method of solution

The Oldroyd-B equations in the periodic steady-state are solved as just described using a mixed pseudo-spectral / finite differences approach. To begin, all variables are described in a Fourier basis in the azimuthal angle θ,

$$p(r,\theta) = \sum_{k=-N}^{N} \hat{p}_k(r)e^{ik\theta}, \quad \boldsymbol{u}(r,\theta) = \sum_{k=-N}^{N} \hat{\boldsymbol{u}}_k(r)e^{ik\theta}, \quad \boldsymbol{\tau}(r,\theta) = \sum_{k=-N}^{N} \hat{\boldsymbol{\tau}}_k(r)e^{ik\theta}. \tag{26}$$

The radial distance from the filament center, r, is discretized as $r_m = A + (A_{out} - A)((m-1)/M)^2$ for $m = 1, 2, ..., M+1$. Here A_{out} is an outer radial distance taken large enough so that the numerical results are not altered significantly with any further increases in its value. For example, in the helical wave case with $A = 0.5$ and $\psi = \pi/40$ from the main text, it is sufficient to take $A_{out} = 20A$ in order that the errors be due to discretization alone. Moreover, the swimming speed computed using only $M = 200$ and $N = 2$ changes by less than 0.2% with any increases in M or N. For larger pitch angles such as $\psi = \pi/5$, again with $A = 0.5$, we require $A_{out} = 30A$, $M = 200$, and $N = 6$ for comparable precision, with resolution requirements increasing with the Deborah number, and in the study of rigid body rotation. The computational costs required to accurately study bodies of even larger pitch angle were generally found to be prohibitive in the current approach.

The choice of a quadratic scaling in the discretization of r increases the resolution of the fluid velocity and stress near the body where it is most needed. Radial derivatives are computed using fourth-order finite difference formulae derived specifically for the spatially varying grid spacing in r. Formulae for derivatives near the endpoints are skewed, depending upon variable information on the boundary and inside the domain of computation. Azimuthal derivatives, meanwhile, are computed in Fourier space using the definitions in (26).

Iterative scheme

Our approach is to develop an iterative numerical scheme. Initial guesses for the velocity and pressure fields, and the swimming speed, are relaxed until the equations of motion are satisfied. As unknowns we take the Fourier modes (with radial dependence) describing the velocity field $\hat{\boldsymbol{u}}_k(r_m)$ and the pressure $\hat{p}_k(r_m)$,

and also the swimming speed U, which are all formed into a single vector $\boldsymbol{\nu}$ of length $4M(2N+1)+1$. For a given approximation to the velocity field $\boldsymbol{u}$ and swimming speed U, the stress $\boldsymbol{\tau}$ is treated as an auxiliary variable and is determined immediately through the constitutive equation (14). This step is performed rapidly using a Generalized Minimal Residual iterative scheme (GMRES) [3].

The momentum balance equation (9) is required to be satisfied at every radial grid point (collocation), and when integrated against the Fourier basis functions (a Galerkin scheme) [4],

$$\int_0^{2\pi} e^{iK\theta} \left[\nabla p - \nabla \cdot \boldsymbol{\tau}\right](r_m, \theta)\, d\theta = 0, \tag{27}$$

for $m = 1, 2..., M+1$, and for $K = -N, -N+1, ..., N-1, N$. The momentum balance equation is replaced by the no-slip boundary conditions for the velocity field on the innermost and outermost radial gridpoints. Simultaneously we require that

$$\int_0^{2\pi} e^{iK\theta} \left[\boldsymbol{\Delta} p - \nabla \cdot (\nabla \cdot \boldsymbol{\tau}_p)\right](r_m, \theta)\, d\theta = 0, \tag{28}$$

again for each radial gridpoint and against each Fourier basis function. To derive the above we have used the mass conservation equation $\nabla \cdot \boldsymbol{u} = 0$. This equation is replaced by the following boundary conditions at the innermost and outermost radial boundaries,

$$\left.\frac{\partial p}{\partial r}\right|_{r=A} = -(\eta_s/\eta)\, \hat{\boldsymbol{r}} \cdot (\nabla \times \nabla \times \boldsymbol{u}) + \left.\hat{\boldsymbol{r}} \cdot (\nabla \cdot \boldsymbol{\tau}_p)\right|_{r=A}, \tag{29}$$

$$\left.\frac{1}{r}\frac{\partial p}{\partial \theta}\right|_{r=A_{out}} = -(\eta_s/\eta)\, \hat{\boldsymbol{\theta}} \cdot (\nabla \times \nabla \times \boldsymbol{u}) + \left.\hat{\boldsymbol{\theta}} \cdot (\nabla \cdot \boldsymbol{\tau}_p)\right|_{r=A_{out}}. \tag{30}$$

Here we are free to assert that the pressure on the outer boundary has mean zero, thereby fixing the constant of integration (which has no bearing on the flow velocity or swimming speed). The condition that the velocity field is divergence free is retained as a diagnostic tool and is verified at the end of each computation.

Finally, we require the net force on the swimming body to be zero, $F_z = 0$ (see (16)). The equations and constraints above are written together as a large nonlinear system of $4M(2N+1)+1$ equations, $\mathcal{F}[\boldsymbol{\nu}] = \boldsymbol{0}$. The solution to this system of equations is found by the application of Broyden's method, an adaptation of Newton's method that updates the Jacobian matrix $\boldsymbol{J} = [\partial \mathcal{F}/\partial \boldsymbol{\nu}]$ at each iteration without recomputing each matrix entry [5]. For the first iteration, the Jacobian is computed using a centered finite difference approximation. $\boldsymbol{J}$ is sparse and fast algorithms for matrix inversion and multiplication are employed. Since each column of $\boldsymbol{J}$ can be determined independent of all other columns, this step is performed in blocks on a parallel architecture without complication. Close initial guesses $\boldsymbol{\nu}^0$ for a given Deborah number are provided by extrapolation from previous computations for smaller De, starting with the simplest computation, that of Stokes flow (De = 0).

To validate the code we have tested against an exact solution of cylindrical helical flow in an annulus, compared to other computations of Newtonian flows, and performed convergence studies in the general setting, all of which indicate the expected numerical accuracy. Extensive details will be provided in a separate manuscript.

II. RHEOLOGICAL AND BIOLOGICAL DATA

We include as Table I a selection of recent experimental investigations of fluid rheological measurements and microorganism geometries. Detailed fluid rheology and microorganism geometries are not generally reported simultaneously in the literature, making a full comparison to the swimming speeds observed in vivo quite challenging. The data shown, however, is generally consistent with our results, in that swimming

in viscoelastic fluids appears to be enhanced for slender filaments of large amplitude (e.g., pitch angle $\psi \gtrsim 30^\circ$ for helical bodies). The organism geometry is reported in Table I as the dimensionless filament radius A. Whether the organism swims faster or slower in a viscoelastic medium than in a Newtonian fluid is indicated as 'relative motility'.

TABLE I. Biological data (*denotes peritrichous cells)

Organism	Kinematics	Filament radius, A	Medium	Relative motility
B. burgdorferi	flat wave, $\psi = 35^\circ$	0.5 [6]	gelatin	faster (no slip) [7]
Mouse sperm (fresh)	small amplitude	0.03 [8, 9]	viscoelastic	slower [10]
Mouse sperm (hyperactivated)	large amplitude	0.03 [8, 9]	viscoelastic	faster [10]
E. coli *	helical, $\psi = 30^\circ$	0.03 [11]	Methocel (gel)	faster [12]
P. aeruginosa	$\psi = 40^\circ$ [13]	0.03	mucin	faster [14]
H. pylori *	/	0.03	PGM† gel (De $\sim 10^3$)	immotile [15]
H. pylori *	helical, $\psi = 57^\circ$	0.03	PGM† solution (De ~ 1)	motile [15]
C. elegans	planar undulation	0.3	CMC†† gel (De ~ 1)	slower [16]

† Porcine gastric mucin †† Carboxy-methyl cellulose solution

We acknowledge Lei Li for helpful comments on this document.

APPENDIX A. DIFFERENTIAL OPERATIONS IN THE HELICAL COORDINATE SYSTEM

From the definition of the helical coordinate system in (3), we now derive a number of differential operators acting on scalars, vectors, and tensors that appear in the equations of motion. Beginning with the relations in (6) and (19) we have that

$$\frac{\partial}{\partial r}\hat{\boldsymbol{r}} = 0, \quad \frac{\partial}{\partial r}\hat{\boldsymbol{\theta}} = 0, \tag{31}$$

$$\frac{\partial}{\partial \theta}\hat{\boldsymbol{r}} = \hat{\boldsymbol{\theta}}, \quad \frac{\partial}{\partial \theta}\hat{\boldsymbol{\theta}} = -\hat{\boldsymbol{r}}, \tag{32}$$

$$\frac{\partial}{\partial z}\hat{\boldsymbol{r}} = -\frac{\beta\cos(\theta)}{\alpha\, r}\hat{\boldsymbol{\theta}}, \quad \frac{\partial}{\partial z}\hat{\boldsymbol{\theta}} = \frac{\beta\cos(\theta)}{\alpha\, r}\hat{\boldsymbol{r}}. \tag{33}$$

As was stated previously, the gradient of any scalar variable such as the pressure (with $\partial p/\partial\zeta = 0$ assumed) is given using (21), and the divergence of a vector is given as in (23). Similarly, using the del operator shown in (20), the curl of a vector $\boldsymbol{u} = u\hat{\boldsymbol{r}} + v\hat{\boldsymbol{\theta}} + w\hat{\boldsymbol{z}}$ is seen to be

$$\nabla\times\boldsymbol{u} = \hat{\boldsymbol{r}}\left(\frac{1}{r}\frac{\partial w}{\partial\theta} - \frac{\partial v}{\partial z} + \frac{\beta\cos(\theta)}{\alpha r}u\right) + \hat{\boldsymbol{\theta}}\left(-\frac{\partial w}{\partial r} + \frac{\partial u}{\partial z} + \frac{\beta\cos(\theta)}{\alpha r}v\right) + \hat{\boldsymbol{z}}\left(\frac{\partial v}{\partial r} + \frac{v}{r} - \frac{\partial u}{\partial\theta}\right), \tag{34}$$

and the gradient acting on the velocity vector $\boldsymbol{u}$ is given by

$$\nabla\boldsymbol{u} = \hat{\boldsymbol{r}}\hat{\boldsymbol{r}}\frac{\partial u}{\partial r} + \hat{\boldsymbol{r}}\hat{\boldsymbol{\theta}}\frac{\partial v}{\partial r} + \hat{\boldsymbol{r}}\hat{\boldsymbol{z}}\frac{\partial w}{\partial r} + \frac{1}{r}\left(\hat{\boldsymbol{\theta}}\hat{\boldsymbol{r}}\left[\frac{\partial u}{\partial\theta} - v\right] + \hat{\boldsymbol{\theta}}\hat{\boldsymbol{\theta}}\left[\frac{\partial v}{\partial\theta} + u\right] + \hat{\boldsymbol{\theta}}\hat{\boldsymbol{z}}\frac{\partial w}{\partial\theta}\right) \tag{35}$$

$$+\hat{\boldsymbol{z}}\hat{\boldsymbol{r}}\left[\frac{\partial u}{\partial z} + \frac{\beta\cos(\theta)}{\alpha\, r}v\right] + \hat{\boldsymbol{z}}\hat{\boldsymbol{\theta}}\left[\frac{\partial v}{\partial z} - \frac{\beta\cos(\theta)}{\alpha\, r}u\right] + \hat{\boldsymbol{z}}\hat{\boldsymbol{z}}\frac{\partial w}{\partial z}. \tag{36}$$

Here we have described a second-order tensor in terms of dyadic products, for instance $\hat{\boldsymbol{r}}\hat{\boldsymbol{\theta}} = \hat{\boldsymbol{r}} \otimes \hat{\boldsymbol{\theta}} = \hat{\boldsymbol{r}}\hat{\boldsymbol{\theta}}^T$ [1]. To determine tensor derivatives we first note that

$$\partial_\theta(\hat{\boldsymbol{r}}\hat{\boldsymbol{r}}) = -\partial_\theta(\hat{\boldsymbol{\theta}}\hat{\boldsymbol{\theta}}) = \hat{\boldsymbol{r}}\hat{\boldsymbol{\theta}} + \hat{\boldsymbol{\theta}}\hat{\boldsymbol{r}}, \quad \partial_\theta(\hat{\boldsymbol{r}}\hat{\boldsymbol{\theta}}) = \partial_\theta(\hat{\boldsymbol{\theta}}\hat{\boldsymbol{r}}) = \hat{\boldsymbol{\theta}}\hat{\boldsymbol{\theta}} - \hat{\boldsymbol{r}}\hat{\boldsymbol{r}}, \tag{37}$$

$$\partial_\theta(\hat{\boldsymbol{r}}\hat{\boldsymbol{z}}) = \hat{\boldsymbol{\theta}}\hat{\boldsymbol{z}}, \quad \partial_\theta(\hat{\boldsymbol{z}}\hat{\boldsymbol{r}}) = \hat{\boldsymbol{z}}\hat{\boldsymbol{\theta}}, \quad \partial_\theta(\hat{\boldsymbol{\theta}}\hat{\boldsymbol{z}}) = -\hat{\boldsymbol{r}}\hat{\boldsymbol{z}}, \quad \partial_\theta(\hat{\boldsymbol{z}}\hat{\boldsymbol{\theta}}) = -\hat{\boldsymbol{z}}\hat{\boldsymbol{r}}, \tag{38}$$

$$\frac{\partial}{\partial z}(\hat{\boldsymbol{r}}\hat{\boldsymbol{r}}) = -\frac{\partial}{\partial z}(\hat{\boldsymbol{\theta}}\hat{\boldsymbol{\theta}}) = -\frac{\beta\cos(\theta)}{\alpha\, r}(\hat{\boldsymbol{r}}\hat{\boldsymbol{\theta}} + \hat{\boldsymbol{\theta}}\hat{\boldsymbol{r}}), \tag{39}$$

$$\frac{\partial}{\partial z}(\hat{\boldsymbol{r}}\hat{\boldsymbol{\theta}}) = \frac{\partial}{\partial z}(\hat{\boldsymbol{\theta}}\hat{\boldsymbol{r}}) = -\frac{\beta\cos(\theta)}{\alpha\, r}(\hat{\boldsymbol{\theta}}\hat{\boldsymbol{\theta}} - \hat{\boldsymbol{r}}\hat{\boldsymbol{r}}), \tag{40}$$

$$\frac{\partial}{\partial z}(\hat{\boldsymbol{r}}\hat{\boldsymbol{z}}) = -\frac{\beta\cos(\theta)}{\alpha\, r}\hat{\boldsymbol{\theta}}\hat{\boldsymbol{z}}, \quad \frac{\partial}{\partial z}(\hat{\boldsymbol{z}}\hat{\boldsymbol{r}}) = -\frac{\beta\cos(\theta)}{\alpha\, r}\hat{\boldsymbol{z}}\hat{\boldsymbol{\theta}}, \tag{41}$$

$$\frac{\partial}{\partial z}(\hat{\boldsymbol{\theta}}\hat{\boldsymbol{z}}) = \frac{\beta\cos(\theta)}{\alpha\, r}\hat{\boldsymbol{r}}\hat{\boldsymbol{z}}, \quad \frac{\partial}{\partial z}(\hat{\boldsymbol{z}}\hat{\boldsymbol{\theta}}) = \frac{\beta\cos(\theta)}{\alpha\, r}\hat{\boldsymbol{z}}\hat{\boldsymbol{r}}. \tag{42}$$

Writing a two dimensional tensor $\boldsymbol{A}$ (for example, the rate-of-strain tensor $\boldsymbol{A} = \dot{\boldsymbol{\gamma}}$) as

$$\boldsymbol{A} = A_{rr}\hat{\boldsymbol{r}}\hat{\boldsymbol{r}} + A_{r\theta}\hat{\boldsymbol{r}}\hat{\boldsymbol{\theta}} + A_{rz}\hat{\boldsymbol{r}}\hat{\boldsymbol{z}} + A_{\theta r}\hat{\boldsymbol{\theta}}\hat{\boldsymbol{r}} + A_{\theta\theta}\hat{\boldsymbol{\theta}}\hat{\boldsymbol{\theta}} + A_{\theta z}\hat{\boldsymbol{\theta}}\hat{\boldsymbol{z}} + A_{zr}\hat{\boldsymbol{z}}\hat{\boldsymbol{r}} + A_{z\,\theta}\hat{\boldsymbol{z}}\hat{\boldsymbol{\theta}} + A_{zz}\hat{\boldsymbol{z}}\hat{\boldsymbol{z}}, \tag{43}$$

then the divergence of $\boldsymbol{A}$ may be written as

$$\nabla \cdot \boldsymbol{A} = \left(\hat{\boldsymbol{r}}\partial_r + \hat{\boldsymbol{\theta}}\frac{1}{r}\partial_\theta + \hat{\boldsymbol{z}}\frac{\partial}{\partial z}\right) \cdot \boldsymbol{A}, \tag{44}$$

leading to the following components of the divergence in the locally orthogonal basis $(\hat{\boldsymbol{r}}, \hat{\boldsymbol{\theta}}, \hat{\boldsymbol{z}})$:

$$\hat{\boldsymbol{r}} \cdot [\nabla \cdot \boldsymbol{A}] = \partial_r(A_{rr}) + \frac{1}{r}\partial_\theta(A_{\theta r}) + \frac{\partial}{\partial z}(A_{zr}) + \frac{1}{r}(A_{rr} - A_{\theta\theta}) + \frac{\beta\cos(\theta)}{\alpha\, r}A_{z\theta}, \tag{45}$$

$$\hat{\boldsymbol{\theta}} \cdot [\nabla \cdot \boldsymbol{A}] = \partial_r(A_{r\theta}) + \frac{1}{r}\partial_\theta(A_{\theta\theta}) + \frac{\partial}{\partial z}(A_{z\theta}) + \frac{1}{r}(A_{r\theta} + A_{\theta\, r}) - \frac{\beta\cos(\theta)}{\alpha\, r}A_{z\, r}, \tag{46}$$

$$\hat{\boldsymbol{z}} \cdot [\nabla \cdot \boldsymbol{A}] = \partial_r(A_{rz}) + \frac{1}{r}\partial_\theta(A_{\theta z}) + \frac{\partial}{\partial z}(A_{zz}) + \frac{1}{r}A_{rz}. \tag{47}$$

Finally, since

$$\boldsymbol{u} \cdot \nabla = u\frac{\partial}{\partial r} + \frac{v}{r}\frac{\partial}{\partial \theta} + w\frac{\partial}{\partial z}, \tag{48}$$

we have (using dyadic notation),

$$\hat{\boldsymbol{r}}\hat{\boldsymbol{r}} \cdot [\boldsymbol{u} \cdot \nabla\boldsymbol{A}] = \boldsymbol{u} \cdot \nabla A_{rr} + \Psi(A_{r\theta} + A_{\theta r}), \tag{49}$$

$$\hat{\boldsymbol{r}}\hat{\boldsymbol{\theta}} \cdot [\boldsymbol{u} \cdot \nabla\boldsymbol{A}] = \boldsymbol{u} \cdot \nabla A_{r\theta} - \Psi(A_{rr} - A_{\theta\theta}), \tag{50}$$

$$\hat{\boldsymbol{r}}\hat{\boldsymbol{z}} \cdot [\boldsymbol{u} \cdot \nabla\boldsymbol{A}] = \boldsymbol{u} \cdot \nabla A_{rz} + \Psi A_{\theta z}, \tag{51}$$

$$\hat{\boldsymbol{\theta}}\hat{\boldsymbol{r}} \cdot [\boldsymbol{u} \cdot \nabla\boldsymbol{A}] = \boldsymbol{u} \cdot \nabla A_{\theta\, r} - \Psi(A_{rr} - A_{\theta\theta}), \tag{52}$$

$$\hat{\boldsymbol{\theta}}\hat{\boldsymbol{\theta}} \cdot [\boldsymbol{u} \cdot \nabla\boldsymbol{A}] = \boldsymbol{u} \cdot \nabla A_{\theta\theta} - \Psi(A_{r\theta} + A_{\theta r}), \tag{53}$$

$$\hat{\boldsymbol{\theta}}\hat{\boldsymbol{z}} \cdot [\boldsymbol{u} \cdot \nabla\boldsymbol{A}] = \boldsymbol{u} \cdot \nabla A_{\theta z} - \Psi A_{rz}, \tag{54}$$

$$\hat{\boldsymbol{z}}\hat{\boldsymbol{r}} \cdot [\boldsymbol{u} \cdot \nabla\boldsymbol{A}] = \boldsymbol{u} \cdot \nabla A_{zr} + \Psi A_{z\theta}, \tag{55}$$

$$\hat{\boldsymbol{z}}\hat{\boldsymbol{\theta}} \cdot [\boldsymbol{u} \cdot \nabla\boldsymbol{A}] = \boldsymbol{u} \cdot \nabla A_{z\theta} - \Psi A_{zr}, \tag{56}$$

$$\hat{\boldsymbol{z}}\hat{\boldsymbol{z}} \cdot [\boldsymbol{u} \cdot \nabla\boldsymbol{A}] = \boldsymbol{u} \cdot \nabla A_{zz}, \tag{57}$$

where

$$\Psi = \left[\frac{\beta \cos(\theta)}{\alpha\, r} w - \frac{v}{r} \right]. \tag{58}$$

* spagnolie@math.wisc.edu

[1] R. B. Bird, R. C. Armstrong, and O. Hassager. *Dynamics of polymeric liquids. Vol. 1: Fluid mechanics*. John Wiley and Sons Inc., New York, NY, 1987.

[2] R. G. Larson. *The Structure and Rheology of Complex Fluids*, volume 1. Oxford University Press, 1999.

[3] Y. Saad and M. H. Schultz. GMRES: A generalized minimal residual algorithm for solving nonsymmetric linear systems. *SIAM J. Sci. Stat. Comp.*, 7:856–869, 1986.

[4] K. Atkinson and W. Han. *Theoretical Numerical Analysis*. Springer, New York, NY, 2009.

[5] C. G. Broyden. A class of methods for solving nonlinear simultaneous equations. *Math. Comput.*, 19:577–593, 1965.

[6] J. Yang, C. W. Wolgemuth, and G. Huber. Kinematics of the Swimming of Spiroplasma. *Phys. Rev. Lett.*, 102:218102, 2009.

[7] M. W. Harman, S. M. Dunham-Ems, M. J. Caimano, A. A. Belperron, L. K. Bockenstedt, H. C. Fu, J. D. Radolf, and C. W. Wolgemuth. The heterogeneous motility of the Lyme disease spirochete in gelatin mimics dissemination through tissue. *PNAS*, 109:3059–3064, 2012.

[8] J. M. Cummins and P. F. Woodall. On mammalian sperm dimensions. *J. Reprod. Fert.*, 75:153–175, 1985.

[9] J. M. Baltz, P. O. Willams, and R. A. Cone. Dense fibers protect mammalian sperm against damage. 43(3):485–491, 1990.

[10] S. S. Suarez and X. Dai. Hyperactivation enhances mouse sperm capacity for penetrating viscoelastic media. *Biol. Reprod.*, 46:686–691, 1992.

[11] N. Darnton, L. Turner, K. Breuer, and H. C. Berg. Moving fluid with bacterial carpets. *Biophys. J.*, 86(3):1863–1870, 2004.

[12] H. C. Berg and L. Turner. Movement of microorganisms in viscous environments. *Nature*, 278:349–351, 1979.

[13] A. Verma, S. K. Arora, S. K. Kuravi, and R. Ramphal. Roles of Specific Amino Acids in the N Terminus of Pseudomonas aeruginosa Flagellin and of Flagellin Glycosylation in the Innate Immune Response. *Infect. Immun.*, 73(12):8237–8246, 2005.

[14] M. Caldara, R. S. Friedlander, N. L. Kavanaugh, J. Aizenberg, K. R. Foster, and K. Ribbeck. Mucin biopolymers prevent bacterial aggregation by retaining cells in the free-swimming state. *Current Biol.*, 22:2325–2330, 2012.

[15] J. P. Celli, B. S. Turner, N. H. Afdhal, S. Keates, I. Ghiran, C. P. Kelly, R. H. Ewoldt, G. H. McKinley, P. So, S. Erramilli, et al. Helicobacter pylori moves through mucus by reducing mucin viscoelasticity. *PNAS*, 106:14321–14326, 2009.

[16] X. N. Shen and P. E. Arratia. Undulatory swimming in viscoelastic fluids. *Phys. Rev. Lett.*, 106:208101, 2011.